PHYSICAL REVIEW FLUIDS **4**, 014602 (2019)

Influence of spanwise rotation and scalar boundary conditions on passive scalar transport in turbulent channel flow

Geert Brethouwer*
Linné FLOW Centre, KTH Mechanics, SE-10044 Stockholm, Sweden

(Received 25 June 2018; published 14 January 2019)

Direct numerical simulations of passive scalar transport in turbulent channel flow subject to spanwise rotation are carried out with two different boundary conditions for the scalar. In the first case the scalar transport is driven by an assigned scalar difference at the walls and in the second case by a constant mean streamwise scalar gradient. The Reynolds number $\mathrm{Re} = U_b h/\nu$ is fixed at 14 000 and the rotation number $\mathrm{Ro} = 2\Omega h/U_b$ is varied from 0 to 0.75, where U_b is the mean bulk velocity, h half the channel gap width, and Ω the rotation rate. This work is a continuation of Brethouwer [J. Fluid Mech. **844**, 297 (2018)] to further study the influence of rotation and also the influence of scalar boundary conditions on scalar transport in channel flow. Mean scalar profiles and other scalar statistics differ in the two cases with different boundary conditions but are similar in the near-wall region in terms of local wall units. The conclusion of Brethouwer that the Reynolds analogy for scalar-momentum transfer does not apply to rotating channel flow is independent of scalar boundary conditions. Rotation influences the turbulent scalar flux differently than the Reynolds shear stress and strongly reduces the turbulent Prandtl number on the unstable channel side, irrespective of the scalar boundary conditions. Scalar structures are larger than the turbulence structures in rotating channel flow, in contrast to nonrotating channel flow where these are similar.

DOI: 10.1103/PhysRevFluids.4.014602

I. INTRODUCTION

The influence of rotation on heat and mass transfer in turbulent wall-bounded flows is of practical interest, for example, for turbomachinery, and of theoretical interest. Passive scalar transport in nonrotating turbulent wall-bounded flows has been studied extensively. Pirozzoli *et al.* [1] have recently studied passive scalar transport in nonrotating turbulent channel flow at friction Reynolds numbers $\mathrm{Re}_\tau = u_\tau h/\nu$ up to 4088 and for Prandtl numbers $\mathrm{Pr} = \nu/\alpha$ from 0.2 to 1 by direct numerical simulation (DNS). Here, u_τ is the friction velocity, h half the channel gap width, ν the viscosity, and α the scalar diffusivity. The mean scalar profiles displayed a logarithmic profile in the overlap region and large-scale scalar structures were observed. The turbulent Prandtl number Pr_t varied with Pr and Re_τ but was in general near unity, suggesting that the Reynolds analogy for momentum and scalar transfer applies. Abe and Antonia [2] found that the streamwise velocity and passive scalar fluctuations and other velocity-scalar statistics are strongly correlated near the wall in DNS of turbulent channel flows. Antonia *et al.* [3] observed that the turbulence and passive scalar spectra are fairly similar near the wall and in the outer region, providing further support for the Reynolds analogy. Visualizations, however, suggested that the large-scale scalar structures are wider in the spanwise direction than the streamwise velocity structures, although this was not clearly reflected by the spectra. Also the inclination angles of the large-scale scalar structures with respect to the wall were larger than those of the streamwise velocity structures. More references

---

*geert@mech.kth.se

to studies of turbulent scalar transport and heat transfer in wall-bounded flows can be found in the aforementioned publications.

Physical transport phenomena in turbulent wall-bounded flows subject to rotation have been investigated in much less depth. Passive scalar transport in turbulent channel flow subject to spanwise rotation has been examined by DNS at rotation numbers $\mathrm{Ro} = 2\Omega h/U_b \lesssim 0.5$, and $\mathrm{Re}_\tau = 150$ and 194 by Nagano and Hattori [4] and Liu and Lu [5]. Here, Ω is the rotation rate and U_b the mean bulk velocity. Spanwise rotation tends to augment turbulence on the so-called pressure side or unstable side where rotation is anticyclonic, and to suppress it on the so-called suction or stable side where rotation is cyclonic [6,7]. This naturally leads to slow and fast turbulent scalar transport on the stable, respectively, unstable, channel side [4,5]. Rotation also reduces the streamwise turbulent scalar flux in the outer region and Nusselt number Nu [5]. Wu and Kasagi [8] carried out DNS of turbulent channel flow with a passive scalar at $\mathrm{Re} = U_b h/\nu = 2280$ with varying directions of the rotation axis and observed a large influence of rotation on the turbulent scalar flux direction and mean scalar gradients. DNS of turbulent passive scalar transport in a square duct flow subject to spanwise rotation was carried out by Fang and Wang [9]. Also in this case, the influence of rotation on the scalar fluxes and Nu were considerable.

These studies were mostly at low Reynolds numbers. Recently, I have studied passive scalar transport in spanwise rotating turbulent channel flow at a higher $\mathrm{Re} = 20\,000$, and $\mathrm{Ro} \leqslant 1.2$ through DNS [10]. At high Ro turbulent scalar transport is strongly reduced on the stable side since the flow relaminarizes there. A main finding was that the Reynolds analogy does not apply to rotating channel flow since the turbulent scalar transfer is often much faster than the momentum transfer on the unstable channel side. This is reflected by Pr_t, which in some parts of the channel becomes smaller than 0.2 at higher Ro. Spectra showed that the scalar and the turbulent scales also differ in rotating channel flow. Some of the rotation effects on scalar transport in channel flow are also seen in rapid distortion theory and DNS of homogeneous turbulent shear flow subject to rotation [11,12].

There have been several attempts to model heat and mass transfer in rotating wall-bounded flows. Large-eddy simulation (LES) with the lattice Boltzmann method can capture the effects of spanwise rotation on passive scalar transport in turbulent channel flow at low Ro quite well [13], but accurately predicting turbulent scalar transport at higher Ro is likely challenging since predicting the flow at high Ro by LES is hard [14]. Attempts have also been made with Reynolds-averaged models [15], but the model results deviate sometimes strongly from DNS [16,17], demonstrating that better models are welcome.

In previous DNS of passive scalar transport in spanwise rotating channel flow scalar transport was forced by an assigned scalar difference at the two walls, which leads to a mean scalar gradient in the wall-normal direction [4,5,10]. In DNS of nonrotating channel flow also other scalar boundary conditions have been used. Kim and Moin [18] studied a case with the scalar put to zero at the walls and a constant forcing term in the scalar transport equation. Pirozzoli *et al.* [1] studied the same case and the case with an assigned scalar difference. The two cases gave similar results near the walls in terms of wall units, but in the outer layer the differences were considerable. In the constant forcing case the scaled scalar fluctuations were much weaker and the turbulent Prandtl number deviated more from unity in the center region of the channel implying a greater difference between momentum and scalar transfer. Abe and Antonia [2], Antonia *et al.* [3], Kasagi *et al.* [19], Abe and Antonia [20], Lluesma-Rodríguez *et al.* [21] studied a case with a constant streamwise mean scalar gradient. This case is, like the assigned difference case, in principle reproducible in experiments. Kawamura *et al.* [22] compared these two cases in DNS of nonrotating channel flow at $\mathrm{Re}_\tau = 180$. At this low Reynolds number the scalar statistics were not only different in the outer region but also closer to the wall. Obviously, boundary conditions have a noticeable impact on scalar statistics and the similarity between momentum and scalar transfer.

The aim of this study is to investigate passive scalar transport in fully developed turbulent channel flow subject to spanwise rotation and examine the influence of the scalar boundary conditions on the scalar statistics by comparing the case with an assigned scalar difference at the walls to the case with an imposed mean streamwise scalar gradient.

The aims are (i) to answer the key question if the previous conclusion about the failure of the Reynolds analogy in rotating channel flow [10] is affected by the scalar boundary conditions, (ii) to compare the two cases with different scalar boundary conditions, and (iii) to further investigate the difference between turbulent scalar and momentum transfer in rotating channel flow. For this study I use DNS at $\mathrm{Re} = 14\,000$ corresponding to $\mathrm{Re}_\tau = 730$ in the nonrotating case and vary Ro from 0 to 0.75. This Re_τ is higher than in the study of Kawamura *et al.* [22] so that I can examine if the previously observed near-wall differences of the scalar statistics for the assigned scalar difference and imposed mean streamwise scalar gradient cases also exist at higher Reynolds numbers. The computed statistics can support modeling of turbulent heat and mass transfer in rotating wall-bounded flows.

II. NUMERICAL PROCEDURE

Statistically stationary cases of rotating turbulent channel flow with a passive scalar with different scalar boundary conditions are considered. In the following x, y, and z are the streamwise, wall-normal, and spanwise coordinate, respectively. In the first case with an assigned scalar difference, called case 1, the scalar is constant but has a different value at the walls. The scalar Θ' is governed by

$$\frac{\partial \Theta'}{\partial t} + \mathbf{U}'\cdot\nabla\Theta' = \frac{1}{\mathrm{Pr}\,\mathrm{Re}}\nabla^2\Theta' + Q \tag{1}$$

with $Q = 0$ and $\Theta' = 0$ at one wall at $y = -1$ and $\Theta' = 1$ at the other wall at $y = 1$. The equation is made dimensionless with U_b and h. From Eq. (1) follows that the mean scalar fluxes are constant and equal at both walls in the statistically stationary state, irrespective if the channel is rotating or not.

In the second case, called case 2, the scalar at the wall grows linearly with x. For a fully developed flow and scalar field the mean streamwise temperature gradient is then constant and equal at all y [19]. Defining $T = Gx - \Theta'$, where T is the total scalar and G the mean streamwise scalar gradient, it can be shown that the deviation Θ' from the local wall temperature obeys Eq. (1) with $Q = G'U'$ where G' and U' are the dimensionless streamwise mean scalar gradient and velocity, respectively. At the walls the boundary condition is $\Theta' = 0$ implying that there are no scalar fluctuations at the walls and that the two walls have the same temperature. Also in this case, the mean scalar fluxes are constant at the walls, but they are different at $y = -1$ and $y = 1$ when the channel rotates. Nevertheless, from Eq. (1) with $Q = G'U'$ (note that U' is scaled by U_b) one can derive by integration for the average of the mean wall scalar gradients

$$\frac{1}{2}\left[\left(\frac{\partial\Theta}{\partial y}\right)_{y=-1} - \left(\frac{\partial\Theta}{\partial y}\right)_{y=1}\right] = \mathrm{Pr}\,\mathrm{Re}\,G', \tag{2}$$

where $(\partial\Theta/\partial y)_{y=-1}$ and $(\partial\Theta/\partial y)_{y=1}$ are the mean wall scalar gradients at $y = -1$ and 1, respectively. Case 1, with scalar transport driven by a mean wall-normal scalar gradient, has been studied in nonrotating channel flow by, e.g., Johansson and Wikström [23] and in rotating channel flow by, e.g., Nagano and Hattori [4], Brethouwer [10]. Case 2, with scalar transport driven by a mean streamwise scalar gradient, has been studied by, e.g., Kasagi *et al.* [19], Kawamura *et al.* [24] in nonrotating channel flow.

The advection-diffusion equations (1) for the two cases are solved together with the incompressible Navier-Stokes equations with the same pseudospectral code as in Brethouwer [7,10] using Fourier expansions in the x and z directions and Chebyshev polynomials in the y direction. The channel is subject to system rotation about the spanwise direction and periodic boundary conditions are used for the velocity and scalars in the x and z directions. A figure of the flow geometry and coordinate system is shown in Brethouwer [10]. The flow rate is kept constant so that $\mathrm{Re} = 14\,000$ in all cases. Ro is varied from 0 to 0.75 and Pr is set to 0.71. The computational domain size is 6π

TABLE I. DNS parameters: $\mathrm{Ro}_\tau = 2\Omega h/u_\tau$, N_x, N_y, and N_z are the number of Fourier and Chebyshev modes in the streamwise, wall-normal, and spanwise direction, respectively.

Ro	Ro_τ	Re_τ	Re_τ^u	Re_τ^s	$N_x \times N_y \times N_z$
0	0	730	730	730	$1024 \times 257 \times 768$
0.15	3.0	709	805	597	$1152 \times 289 \times 800$
0.3	6.5	643	762	496	$1024 \times 257 \times 768$
0.45	10.7	588	713	430	$960 \times 241 \times 640$
0.75	22.1	476	590	323	$768 \times 193 \times 576$

and 2π in the x and z direction, respectively, when normalized by h, which is somewhat smaller than in Brethouwer [10] but the same as in Pirozzoli *et al.* [1]. DNS of Lluesma-Rodríguez *et al.* [21] have shown that for nonrotating channel flow this size is more than sufficient to obtain one-point scalar statistics and budgets that are independent of the domain size. Once the DNS reached a statistically stationary state they were run for a long time, from $612U_b/h$ timescales at $\mathrm{Ro} = 0$ up to $2200U_bh$ timescales at $\mathrm{Ro} = 0.75$, to obtain well converged statistics of the scalar transport. In the DNS the difference between the mean scalar fluxes at the two walls is at most 0.3% in case 1 and the total mean scalar fluxes at the wall deviate at most 0.5% from the mean balance given by Eq. (2) in case 2. DNS parameters are listed in Table I. The friction velocity is calculated as $u_\tau = [u_{\tau u}^2/2 + u_{\tau s}^2/2]^{1/2}$, where $u_{\tau u}$ and $u_{\tau s}$ are the friction velocities of the unstable and stable channel side, respectively, and Re_τ^u and Re_τ^s are the friction Reynolds numbers based on $u_{\tau u}$ and $u_{\tau s}$, respectively. The streamwise and spanwise grid spacing in terms of Fourier modes and wall units of the unstable side is $\Delta x^+ \leqslant 14.5$ and $\Delta z^+ \leqslant 7.0$, respectively, which is similar to the resolution of previous DNS of rotating channel flow [6]. The spanwise resolution $6.0 \leqslant \Delta z^+ \leqslant 6.3$ in the three DNS with the highest Re_τ is the same as in recent high-Reynolds number DNS of turbulent channel flow [25].

III. FLOW FIELD

In this section, I will discuss some features of the flow and scalar field. In the next sections I will discuss the scalar statistics. Statistics derived from case 1 with an assigned scalar difference are denoted by the subscript 1 and statistics derived from case 2 with a streamwise mean scalar gradient are denoted by the subscript 2.

Figure 1 shows the profiles of the mean streamwise velocity U scaled by U_b and the root mean square (rms) of the wall-normal velocity fluctuations v^+ in wall units. The mean velocity shows the typical skewed profile of spanwise rotating turbulent channel flow with a linear part obeying

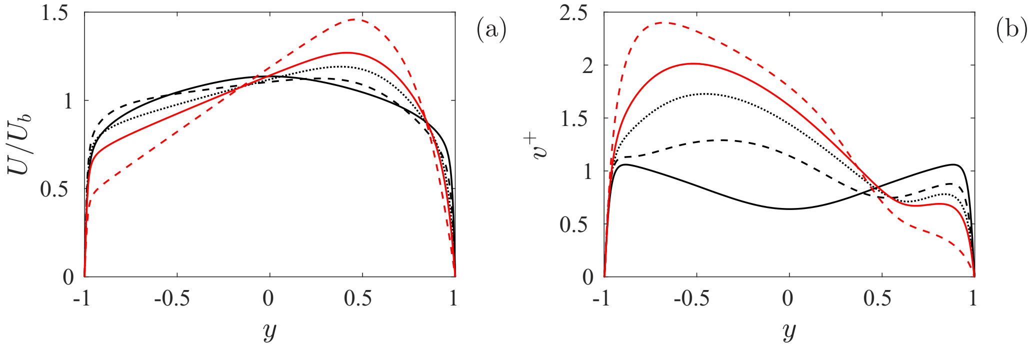

FIG. 1. Profiles of (a) U/U_b and (b) v^+ at $\mathrm{Ro} = 0$ (black solid), $\mathrm{Ro} = 0.15$ (black dashed), $\mathrm{Ro} = 0.3$ (black dotted), $\mathrm{Ro} = 0.45$ (red solid), and $\mathrm{Ro} = 0.75$ (red dashed).

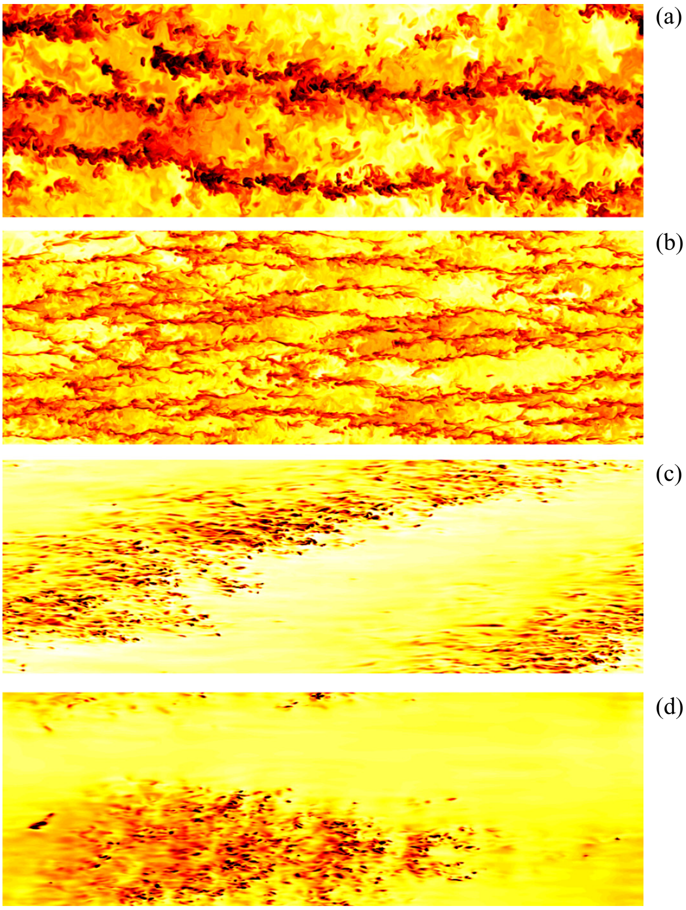

FIG. 2. Visualizations of the scalar field in an x-z plane in case 2 on the unstable channel side at (a) $\mathrm{Ro} = 0.15$ and $y = -0.5$ and (b) $\mathrm{Ro} = 0.75$ and $y = -0.9$. A dark color corresponds to a low scalar value. Visualizations of the instantaneous scalar gradients in case 2 on the stable channel side at the wall at $y = 1$ at (c) $\mathrm{Ro} = 0.3$ and (d) $\mathrm{Ro} = 0.75$. A dark color corresponds to large scalar gradients. The flow is from left to right.

$dU/dy \simeq 2\Omega$ [6]. The unstable (left) side of the channel is strongly turbulent with a growing v^+ with Ro, whereas turbulence on the stable (right) side is suppressed by rotation, leading to a monotonic decline of v^+ with Ro. Figure 2(a) shows a visualization of the scalar field in case 2 at $\mathrm{Ro} = 0.15$ in an x-z plane on the unstable channel side. Streamwise streaks with low scalar values indicate the presence of large streamwise counter-rotating roll cells, as previously observed [7], transporting the scalar away from the wall between the roll cells. Cross-stream visualizations (not shown) confirm that the streaks are caused by large-scale updrafts. Similar streaks are also visible at $\mathrm{Ro} = 0.3$ and 0.45, suggesting that large roll cells are present when $0.15 \leqslant \mathrm{Ro} \leqslant 0.45$. Spectra, not presented here, support this suggestion and further show that the size of the roll cells decreases with Ro. Also at $\mathrm{Ro} = 0.75$ streaks are visible [Fig. 2(b)], but they appear shorter and the spanwise spacing is much smaller, indicating that roll cells are absent or much smaller and lack streamwise coherence, which is supported by the spectra presented later.

The stable channel side is fully turbulent at $\mathrm{Ro} = 0.15$ (not shown) but partly relaminarizes at higher Ro. Figures 2(c) and 2(d) show the instantaneous scalar gradient at the wall on the stable side at $\mathrm{Ro} = 0.3$, and 0.75, respectively. Small-scale fluctuations in the scalar gradient point to turbulence, whereas the absence of those fluctuations imply that the flow is locally laminarlike.

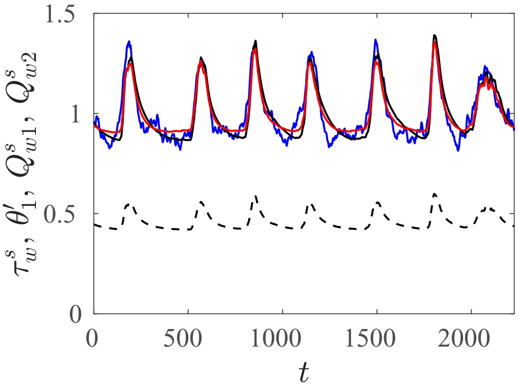

FIG. 3. Time series at $\mathrm{Ro} = 0.75$ of τ_w^s (black dashed), θ_1' (blue solid), Q_{w1}^s (black solid), and Q_{w2}^s (red solid).

From the visualization it can be concluded that patterns in the form of oblique bands of alternating turbulent and laminar flow exist on the stable channel side at $\mathrm{Ro} = 0.3$. Oblique turbulent-laminar patterns are also found at $\mathrm{Ro} = 0.45$ (not shown), but the turbulent band appears somewhat less wide in that case. The patterns persist and are strictly confined to the near-wall region of the stable side. Similar oblique turbulent structures are also found in other transitional wall-bounded flows (see, e.g., Duguet *et al.* [26], Brethouwer *et al.* [27]), although often spanning the whole channel. At a higher $\mathrm{Ro} = 0.75$ a single turbulent spot in a laminarlike environment is seen on the stable side instead of an oblique pattern [Fig. 2(d)]. This spot goes through a continuous cycle of growth and decline, inducing recurring spikes in the mean wall shear stress, τ_w^s, and simultaneous spikes in the mean scalar gradient at the wall on the stable side, $Q_{w1}^s = (\partial\Theta_1/\partial y)_{y=1}$ and $Q_{w2}^s = (\partial\Theta_2/\partial y)_{y=1}$, and the rms of scalar fluctuations in case 1, θ_1', as shown by the time series in Fig. 3. The visualization shown in Fig. 2(d) was obtained when the turbulent spot has approximately its maximum size, corresponding to one of the peaks in Fig. 3. Before each peak the spot almost completely disappears. Similar periodiclike variations in the wall shear stress and wall scalar gradient have been observed in spanwise rotating channel flow by Brethouwer [7,10,28] but the physical mechanism differs. In the latter studies the spikes on the stable channel side result from a recurring linear instability of a Tollmien-Schlichting-like wave, whereas here this wave and thus the linear instability is absent and the spikes are caused by a continuous cycle of growth and decay of a turbulent spot. The latter process is akin to that observed by Hsieh *et al.* [17] in their DNS of spanwise rotating channel flow. The period of the variations of the turbulent spot is also shorter than that related to the linear instability of a Tollmien-Schlichting-like wave. However, it can be that the variations of the turbulent spot largely disappear when the computational domain is substantially enlarged, as observed in other transitional flows [27].

The observations of roll cells on the unstable channel side and partial relaminarization of the flow and oblique patterns and spots on the stable side are consistent with previous studies [7,10]. For further discussions of these structures and flow statistics I refer to these studies and, e.g., Xia *et al.* [6] and Grundestam *et al.* [29]. The flow relaminarization and slow variations of the turbulent spot necessitates long simulations to obtain converged statistics. The periods with the spikes in the turbulent activity on the stable side at $\mathrm{Ro} = 0.75$ are not filtered out, as in Brethouwer [10], but are included in the statistics.

IV. SCALAR STATISTICS

After a brief discussion of the flow and scalar field I turn now to the scalar statistics. Here below, Θ_i denotes the mean scalar, θ_i its fluctuation, and u and v the streamwise and wall-normal velocity fluctuations, respectively.

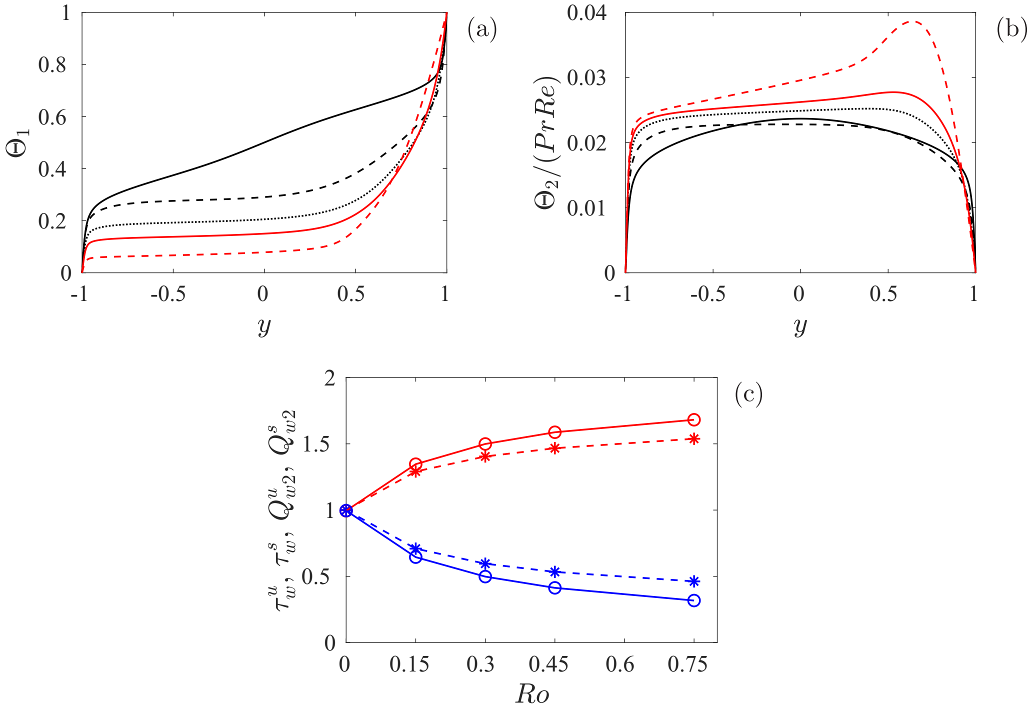

FIG. 4. Profiles of (a) Θ_1 and (b) $\Theta_2/(\mathrm{Pr\,Re})$. Lines as in Fig. 1. (c) τ_w^u/τ_w (red dashed), τ_w^s/τ_w (blue dashed), $Q_{w2}^u/(\mathrm{Pr\,Re})$ (red solid),and $Q_{w2}^s/(\mathrm{Pr\,Re})$ (blue solid) as a function of Ro.

Figures 4(a) and 4(b) show the mean scalar profiles Θ_1 and $\Theta_2/(\mathrm{Pr\,Re})$. The scaling of Θ_2 by Pr Re is inspired by relation (2) noting that in the present DNS $G' = 1$. The Θ_1 profiles are similar as in Brethouwer [10] with a small and large mean scalar gradient on the unstable and stable channel side, respectively, for $\mathrm{Ro} > 0$. This can be motivated by the facts that the scalar flux across the channel is constant in case 1 and the turbulent scalar diffusivity is much smaller on the stable channel side [10]. The Θ_2 profile is naturally symmetric if $\mathrm{Ro} = 0$ but becomes asymmetric under the influence of rotation. It is remarkably flat for $-0.6 \lesssim y \lesssim 0.3$ at $\mathrm{Ro} = 0.15$ and 0.3, and displays a bump on the stable channel side at $\mathrm{Ro} = 0.75$, which is explained later. In contrast to case 1, the scalar fluxes at the two walls are not the same in case 2 if $\mathrm{Ro} > 0$. Figure 4(c) shows the scaled mean wall scalar fluxes $Q_{w2}^u/(\mathrm{Pr\,Re})$ and $Q_{w2}^s/(\mathrm{Pr\,Re})$ in case 2 together with the scaled mean wall shear stresses τ_w^u/τ_w and τ_w^s/τ_w on the unstable and stable side, respectively, where $\tau_w = (\tau_w^u + \tau_w^s)/2$. Note that $Q_{w2}^u + Q_{w2}^s = 2\mathrm{Pr\,Re}$ and is invariant with Ro. Both $Q_{w2}^u/(\mathrm{Pr\,Re})$ and τ_w^u/τ_w monotonically grow and accordingly $Q_{w2}^s/(\mathrm{Pr\,Re})$ and τ_w^s/τ_w decline with Ro owing to the growing difference between the unstable and stable sides. When $\mathrm{Ro} \gtrsim 2$ the whole flow relaminarizes [6,7], implying that Q_{w2}^u and Q_{w2}^s as well as τ_w^u and τ_w^s will converge for very rapid rotation.

Although the profiles of Θ_1 and Θ_2 strongly differ, they are similar near the wall on the unstable side in terms of wall units, as shown in Fig. 5(a). Here and below, y^+ is the wall distance in viscous wall units ν/u_τ. In case 1 the wall scaling is naturally done in terms of $\theta_{\tau 1} = Q_{w1}/u_\tau$, where $Q_{w1} = \alpha(d\Theta_1/dy)_w$ is the mean scalar flux at the wall. In case 2 the choice of the wall scaling is less obvious since the mean scalar fluxes at the two walls differ. For profiles across the channel a global scaling with $\theta_{\tau 2} = (Q_{w2}^s + Q_{w2}^u)/u_\tau$ appears natural, but for near-wall statistics a local scaling with $\theta_{\tau 2}^u = Q_{w2}^u/u_\tau$ and $\theta_{\tau 2}^s = Q_{w2}^s/u_\tau$ on the unstable and stable side, respectively, is a natural choice. In the following the superscript + denotes global scaling using $\theta_{\tau 2}$ and the superscript $*$ denotes local scaling using $\theta_{\tau 2}^u$ and $\theta_{\tau 2}^s$ (together with u_τ in case of fluxes) on the unstable and stable side,

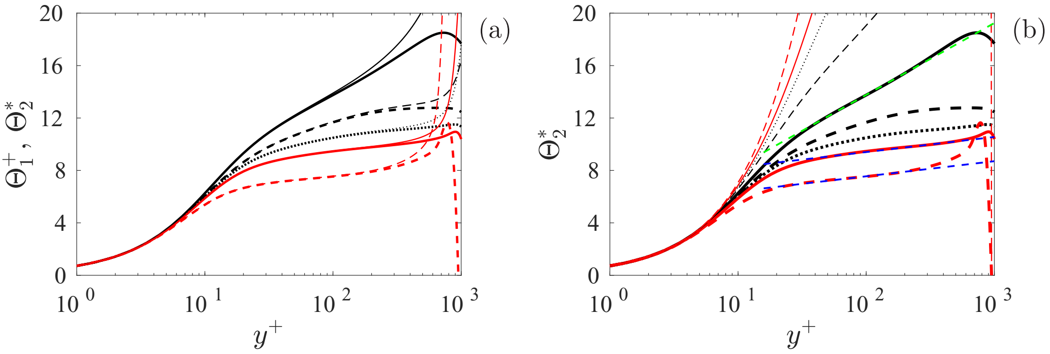

FIG. 5. (a) Profiles of Θ_1^+ (thin lines) and Θ_2^* (thick lines) on the unstable channel side and (b) profiles of Θ_2^* on the stable (thin lines) and unstable channel sides (thick lines). Lines as in Fig. 1. The dashed green and blue lines are explained in the main text.

respectively, in case 2. In case 1 there is no distinction between local and global scaling because the mean wall scalar fluxes are the same at both walls, as said before. Figure 5(a) shows that in local scaling Θ_1^+ and Θ_2^* overlap near the wall on the unstable side at all Ro, underscoring the strong similarities in scalar transport in the two cases. The profiles of Θ_2^* on the stable channel side obviously differ from those at the other side, as shown in Fig. 5(b). On the unstable side, Θ_2^* shows a monotonic decline and on the other side a monotonic growth with Ro since the scalar profiles become more linear when the flow relaminarizes.

In Brethouwer [10], the Θ_1^+ profile in the overlap region on the unstable side at $\mathrm{Ro} = 0$ approximately matches the logarithmic profile

$$\Theta^+ = \frac{1}{\kappa_\theta} \log\, y^+ + C_\theta \tag{3}$$

with $\kappa_\theta = 0.42$ and $C_\theta = 2.8$, given by the dashed green line in Fig. 5(b), whereas at high Ro, Θ_1^+ also approximately match (3) but with $\kappa_\theta = 2.0$, given by the dashed blue lines in Fig. 5(b), and C_θ varying with Ro. Also in the present DNS, the mean scalar profiles on the unstable side at $\mathrm{Ro} = 0$ match (3) with $\kappa_\theta = 0.42$ and $C_\theta = 2.8$. In fact, Θ_2^* better matches this logarithmic profile than Θ_1^+. Lluesma-Rodríguez *et al.* [21] also found that $\kappa_\theta = 0.42$ at $\mathrm{Re}_\tau = 500$ but a slightly higher value of 0.44 at $\mathrm{Re}_\tau = 1000$ and 2000 while Abe and Antonia [20] observed a value of 0.43 at $\mathrm{Re}_\tau = 1020$ in DNS of nonrotating channel flow with the same scalar boundary conditions as case 2 and $\mathrm{Pr} = 0.71$. Abe and Antonia [20] noted that κ_θ increases to 0.46 at higher Re_τ according to the DNS by Pirozzoli *et al.* [1]. Together these studies suggest that κ_θ slowly grows with Re_τ. The profiles of Θ_1^+ and Θ_2^* overlap up to higher y^+ than in the DNS at $\mathrm{Re}_\tau = 180$ by Kawamura *et al.* [22], suggesting that higher Reynolds numbers lead a stronger near-wall similarity in the two cases. At $\mathrm{Ro} = 0.45$ and 0.75 the mean scalar profiles of both cases approximately match (3) with $\kappa_\theta = 2.0$ on the unstable side, whereas the mean velocity profiles do not display this logarithmic behavior [10]. Whether this indicates a genuine logarithmic behavior of the mean scalar profile in rotating channel flow is yet unclear and the physical reason is elusive.

Figure 6(a) shows profiles of θ_2^+ in global scaling. Profiles of θ_1^+ are similar as in Brethouwer [10] and therefore not shown here. There are some variations in θ_2^+ on the unstable side with Ro but no clear trend is visible; the near wall peaks at $0.15 \leqslant \mathrm{Ro} \leqslant 0.45$ are higher than at $\mathrm{Ro} = 0$ and 0.75. On the other hand, on the stable side there is a monotonic decline of θ_2^+ for $y \gtrsim 0.6$ with Ro, which is related to turbulence suppression by rotation. Figures 6(b) and 6(c) show near-wall profiles of θ_2^* together with θ_1^+. In terms of a local scaling θ_2^* shows like Θ_2^* a monotonic decline with Ro on the unstable side. Since the near-wall mean scalar profiles in local scaling collapse on the unstable side at a given Ro we may expect that the near-wall peaks of θ_1^+ and θ_2^* are similar, which is confirmed

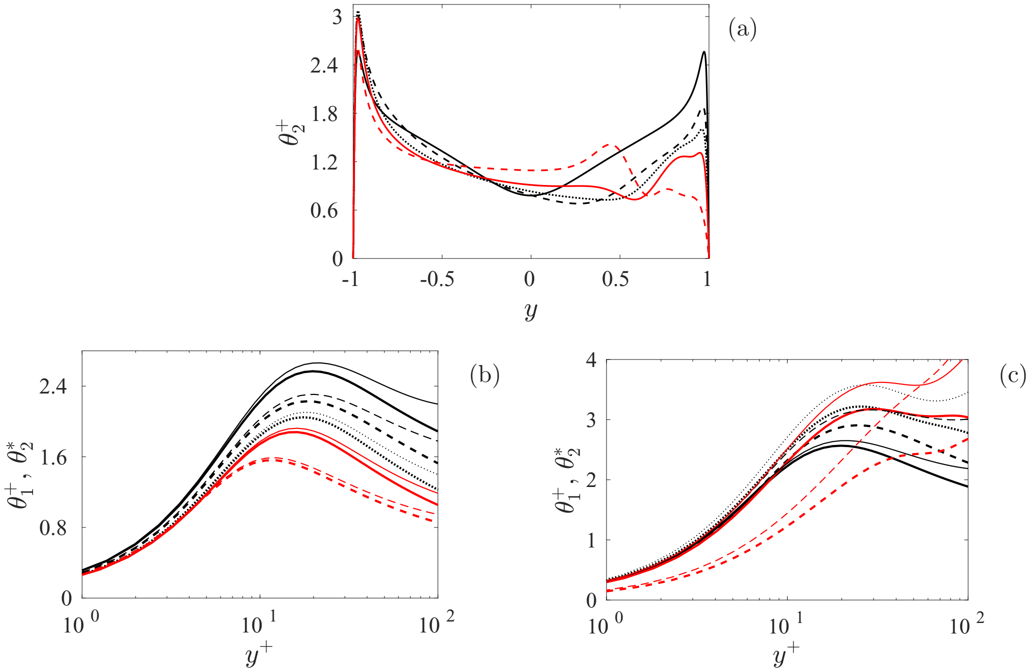

FIG. 6. (a) Profiles of θ_2^+ and (b), (c) near-wall profiles of θ_1^+ (thin lines) and θ_2^* (thick lines) on the unstable and stable channel side, respectively. Lines as in Fig. 1.

by Fig. 6(b). In case 1 the peak is slightly higher, which could be related to the stronger scalar fluctuations in the outer layer in that case, but this difference at $\mathrm{Ro} = 0$ is smaller than at lower Reynolds numbers [22]. Figure 6(c) shows that on the stable side the difference between θ_1^+ and θ_2^* is larger, which is likely caused by the large scalar fluctuations in case 1 away from the wall [see Fig. 7(b) in Brethouwer [10]]. There is no obvious explanation for the variation of the peak values of θ_1^+ and θ_2^* on the unstable side with Ro because the maximal production of scalar energy $\overline{\theta\theta}/2$ given by $P_\theta = -\overline{v\theta}/(\partial\Theta/\partial y)$ (not shown) is in local scaling very close to the theoretical prediction $\mathrm{Pr}/4$ at all Ro [23].

Figure 7(a) shows profiles of the mean streamwise turbulent scalar flux $\overline{u\theta}_2^+$ in global scaling. On the unstable side the near-wall peak of $\overline{u\theta}_2^+$ remains but further away from the wall and on the stable side $\overline{u\theta}_2^+$ decreases with Ro. This behavior on the unstable side is similar to that of $\overline{u\theta}_1^+$ and owing to the effect of the Coriolis term in the balance equation of $\overline{u\theta}$, which counteracts the production term of $\overline{u\theta}$ in the outer region [10]. Figures 7(b) and 7(c) show profiles of the mean streamwise turbulent scalar flux $\overline{u\theta}_1^+$ and $\overline{u\theta}_2^*$ in local scaling near the two walls. Since $\overline{u\theta}_1$ has the opposite sign as $\overline{u\theta}_2$ on the stable side due to the different sign of the mean scalar gradient, $-\overline{u\theta}_1^+$ is plotted in Fig. 7(c). Both $\overline{u\theta}_1^+$ and $\overline{u\theta}_2^*$ decay with Ro on the unstable side near the wall and are very similar, especially at higher Ro when they are indistinguishable. On the stable side by contrast their difference grows with Ro. The decay of the streamwise turbulent scalar flux on the unstable side appears to be related to a similar decay of u^+ with Ro [7].

Figure 8 shows profiles of the mean wall-normal turbulent scalar flux $\overline{v\theta}_2^+$ in global scaling and the correlation coefficient $\rho_{v\theta2} = -\overline{v\theta_2}/(v'\theta_2')$, where v' and θ_2' are the rms of v and θ_2. Profiles of $\overline{v\theta}_1^+$ are not shown since they are similar as in Brethouwer [10]. On the unstable side $\overline{v\theta}_1^+$ is near -1, as follows from the equation for the mean scalar transport across the channel [10], whereas on the stable side this flux is smaller, especially at $\mathrm{Ro} = 0.75$, due to the suppression of turbulence. The

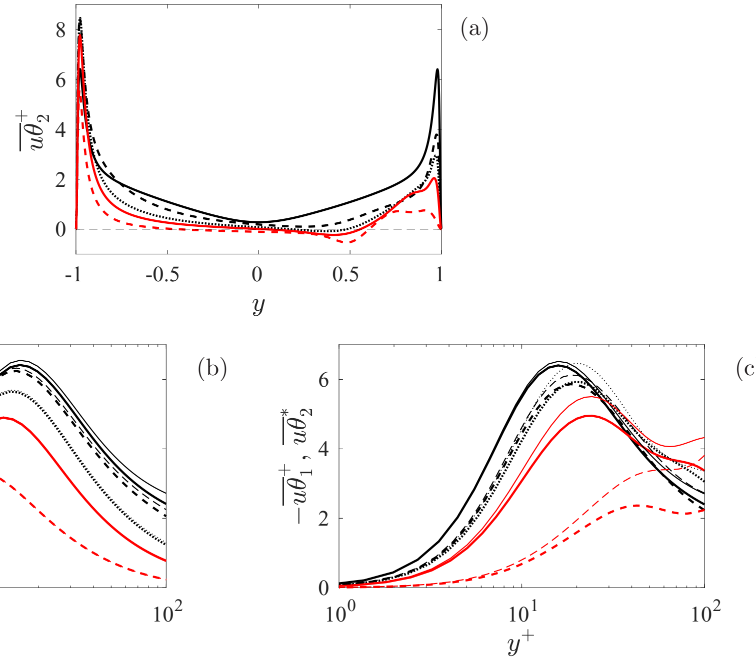

FIG. 7. (a) Profiles of $\overline{u\theta_2}^+$ and (b), (c) near-wall profiles of $\overline{u\theta_1}^+$ (thin lines) and $\overline{u\theta_2}^*$ (thick lines) on the unstable and stable channel side, respectively. (c) Profiles of $-\overline{u\theta_1}^+$ and $\overline{u\theta_2}^*$ on the stable channel side. Lines as in Fig. 1.

profiles of $\overline{v\theta_2}^+$ are clearly different due to another forcing of the scalar field. From Eq. (1) follows after integration that in the steady state

$$-\overline{v\theta_2}^+ = \frac{Q^u_{w2}}{Q_{w2}} - \frac{G'}{Q_{w2}} \int_{-1}^{y} U' dy - \frac{1}{\mathrm{Pr}\,\mathrm{Re}\,Q_{w2}} \frac{\partial \Theta_2}{\partial y}. \tag{4}$$

When the molecular transport term (last term on the right-hand side) is negligible $-\overline{v\theta_2}^+$ is determined by the first two terms on the right-hand side of Eq. (4). The sum of these two terms for each run is shown by the blue lines in Fig. 8(a). The profiles of $-\overline{v\theta_2}^+$ at different Ro closely follow this sum away from the wall, confirming that the statistics are well converged. The wall-normal

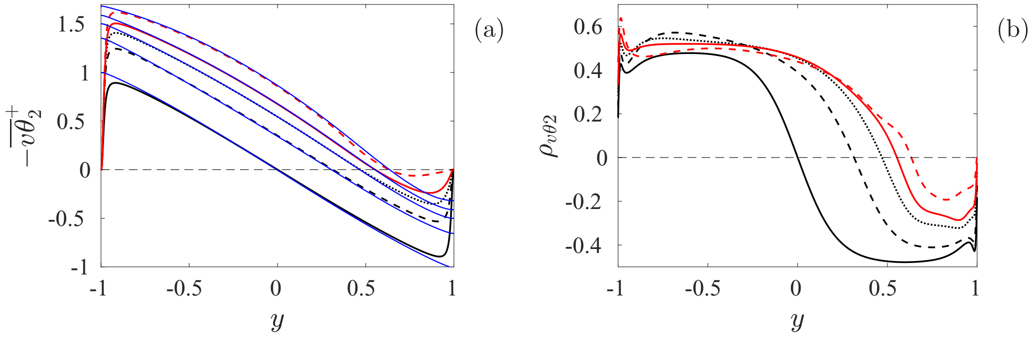

FIG. 8. Profiles of (a) $-\overline{v\theta_2}^+$ and (b) $\rho_{v\theta 2}$. The blue lines show the sum of the first two terms on the right-hand side of Eq. (4). Lines as in Fig. 1.

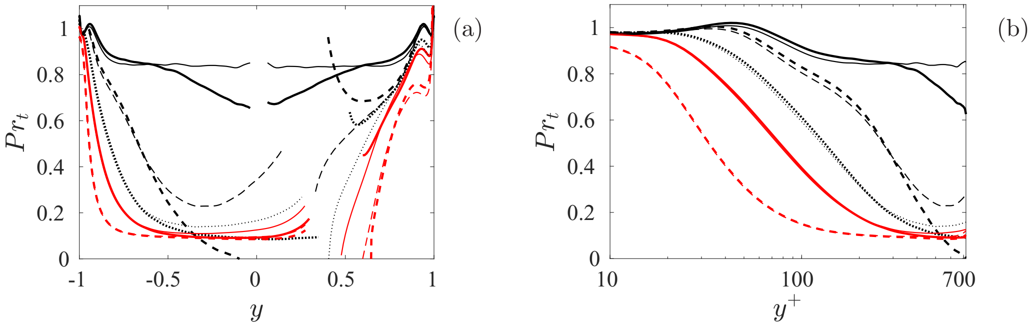

FIG. 9. Profiles of (a) Pr_t and (b) Pr_t on the unstable channel side. Lines as in Fig. 1. The thin lines are for case 1 and the thick lines for case 2.

turbulent scalar flux is, as expected, larger on the unstable side than the stable side, where it strongly declines with Ro. A close inspection shows that at $\mathrm{Ro} = 0.75$, $-\overline{v\theta_2}^+$ is smaller than the sum of the first two terms on the right-hand side of Eq. (4) if $0.4 \lesssim y \lesssim 0.6$. From that follows that the last term in Eq. (4) is negative and therefore $\partial\Theta_2/\partial y$ is positive in this region. This is the cause of the small bump in the profile of Θ_2 at $\mathrm{Ro} = 0.75$ observed in Fig. 4(b) around $y = 0.6$, i.e., molecular transport is not fully negligible there.

The correlation between v and θ_2 is slightly larger at $0.15 \leqslant \mathrm{Ro} \leqslant 0.45$ than at $\mathrm{Ro} = 0$ on the unstable channel side, whereas on the stable side it declines with Ro, showing that rotation has a large impact here on the correlation. A similar conclusion holds for the correlation between v and θ_1 [10]. The decline can be attributed to the influence of the Coriolis term in the transport equation for $\overline{v\theta}$ [10].

V. EFFICIENCY OF TURBULENT SCALAR TRANSPORT

In this section, I consider the efficiency of the turbulent scalar transport, which is especially relevant for modeling and engineering.

A key quantity in many turbulent transport models is the turbulent Prandtl number given by

$$\mathrm{Pr}_{ti} = \frac{\nu_t}{\alpha_{ti}}. \tag{5}$$

The eddy viscosity and scalar diffusivity are here computed as $\nu_t = -\overline{uv}/(dU/dy)$and $\alpha_{ti} = -\overline{v\theta_i}/(d\Theta_i/dy)$, respectively. Pr_{t1} is near unity in nonrotating channel flow in case 1 but much smaller if $\mathrm{Ro} > 0$, in agreement with Brethouwer [10]. Figures 9(a) and 9(b) show Pr_{t1} and Pr_{t2} across the channel and on the unstable channel side. When $dU/dy \simeq 0$ or $d\Theta_i/dy \simeq 0$ there is a discontinuity in Pr_{ti}, which has been removed. Pr_{t1} is about 0.85 in the outer region, in agreement with the DNS of Pirozzoli *et al.* [1], whereas in the center region Pr_{t2} becomes smaller with increasing distance to the wall but stays mostly above 0.7. Elsewhere, for $y \lesssim -0.55$ and $y \gtrsim 0.55$, Pr_{t2} is similar to Pr_{t1}. The Reynolds analogy for momentum and scalar transport is thus approximately valid in case 1 and also case 2, except in the center region of the channel where Pr_{t2} deviates more from unity and the difference between momentum and scalar transfer is noticeable. This difference in the center region of nonrotating channel flow was also noted by Abe and Antonia [20] in DNS with the same scalar boundary conditions as case 2. They suggested that the Reynolds analogy is promoted by the presence of a scalar fluctuation production term. When this production term is small, as in the channel center region in case 2, a larger difference between momentum and scalar transport can be expected, in agreement with the present results. Pirozzoli *et al.* [1] observed only small differences between the turbulent Prandtl number for $\mathrm{Pr} = 0.71$ and 1

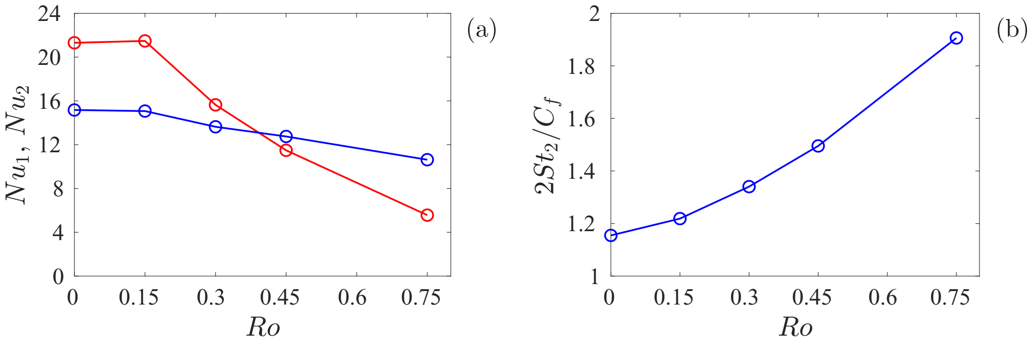

FIG. 10. (a) Nu_1 (red line) and Nu_2 (blue line), and (b) $2\mathrm{St}_2/C_f$ as a function of Ro.

in nonrotating channel flow, showing that Pr has a minor influence on the Reynolds analogy as long as it is near unity.

Both Pr_{t1} and Pr_{t2} drop sharply with Ro in the outer region of the unstable side and are less than 0.2 at higher Ro [Fig. 9(a)], confirming Brethouwer [10]. Only near the wall Pr_{t1} and Pr_{t2} remain near unity. Pr_{t1} and Pr_{t2} are very similar in the wall region $y \lesssim -0.6$ [Figs. 9(a) and 9(b)]. In the center region of the channel Pr_{t2} is smaller than Pr_{t1}, like in the nonrotating case, implying a higher scalar eddy diffusivity and a larger difference between turbulent momentum and scalar transfer. Nevertheless, the strong decline of the turbulent Prandtl number with Ro is observed in both cases 1 and 2 and thus not fundamentally influenced by the scalar boundary conditions. Also on the stable side for $y \geqslant 0.85$, Pr_{t1} and Pr_{t2} decline with Ro but not as much. Further away from the wall both rapidly diminish if $\mathrm{Ro} > 0$. In both cases 1 and 2 the Reynolds analogy is thus clearly invalid and the eddy scalar diffusivity much larger than the eddy viscosity if $\mathrm{Ro} > 0$, meaning that turbulent scalar transfer is much faster than momentum transfer.

Another quantity that reveals the influence of rotation on scalar transport is the Nusselt number, which is defined for cases 1 and 2, respectively, as

$$\mathrm{Nu}_1 = \frac{2h}{\alpha \Delta\Theta} Q_{w1}, \tag{6}$$

$$\mathrm{Nu}_2 = \frac{34}{70} \frac{h}{\alpha \Theta_{2m}} Q_{w2}, \tag{7}$$

where $\Theta_{2m} = \int U\Theta_2 dy/(2hU_b)$ is the mixed mean scalar [1,10,20]. The factors 2 and 34/70 in Eqs. (6) and (7), respectively, are included so that $\mathrm{Nu}_1 = \mathrm{Nu}_2 = 1$ in laminar Poiseuille flow. Figure 10(a) shows Nu_1 and Nu_2 as a function of Ro. Similarly as in Brethouwer [10], Nu_1 at $\mathrm{Ro} = 0$ and 0.15 is approximately the same but then rapidly declines with Ro since the slow transport on the stable side hinders the scalar transport across the channel. Nu_2 shows a slower decline with Ro because the slow scalar transport on the stable side is partly compensated by the rapid transport on the unstable side.

The Reynolds analogy further implies that the ratio of the Stanton number and skin friction coefficient, $2\mathrm{St}_2/C_f$, where $\mathrm{St}_2 = Q_{w2}/(U_b\Theta_{m2})$ and $C_f = 2u_\tau^2/U_b^2$, is near unity [20]. Figure 10(b) shows that $2\mathrm{St}_2/C_f$ is quite close to unity at $\mathrm{Ro} = 0$, confirming that the Reynolds analogy holds for nonrotating channel flow. For $\mathrm{Pr} = 1$, $2\mathrm{St}_2/C_f$ is even closer to unity in nonrotating channel flow [20]. However, $2\mathrm{St}_2/C_f$ monotonically grows with Ro, showing that the Reynolds analogy is invalid for rotating channel flow and that turbulent scalar transfer is rapid compared to momentum transfer, in agreement with previous results. This difference will not disappear if $\mathrm{Pr} = 1$ assuming that the relation between St and Pr does not fundamentally change with Ro. The ratio $2\mathrm{St}_1/C_f$ for case 1 is not shown but was computed for the unstable and stable sides separately by Brethouwer [10]. On the stable side it is near unity but on the unstable side it shows similar behavior as in case 2 with a ratio diverging from unity with Ro, which again highlights the efficient scalar transfer on the unstable side in rotating channel flow.

VI. SPECTRA AND SCALING OF DISSIPATION RATES

In the next part, the length scales of the velocity and scalar field are compared. In nonrotating channel flow, one-dimensional spectra of the velocity and scalar are similar across the channel [3], but this similarity is lost in rotating channel flow away from the wall on the unstable side [10]. To assess if this similarity or difference depends on the scalar boundary conditions, I have computed one-dimensional spanwise spectra of the velocity, $E_K(k_z)$, being the sum of the spectra of the three velocity components, and of the scalars, $E_{\theta\theta}(k_z)$, as well as the one-dimensional streamwise spectra $E_K(k_x)$ and $E_{\theta\theta}(k_x)$, as in Antonia *et al.* [3]. The spectra are scaled, i.e.,

$$\int_0^\infty E_K(k_i)dk_i = 1, \qquad \int_0^\infty E_{\theta\theta}(k_i)dk_i = 1. \tag{8}$$

Figure 11 shows the premultiplied spanwise spectra $k_z E_K(k_z)$ and $k_z E_{\theta\theta}(k_z)$ as a function of λ_z^+ and streamwise spectra $k_x E_K(k_x)$ and $k_x E_{\theta\theta}(k_x)$ as a function of λ_x^+ at $\mathrm{Ro} = 0$, 0.3, and 0.75 at four positions: near the wall at $y^+ \approx 11$ and $y^+ \approx 95$, in the outer region at $y = -0.56$ on the unstable side, and at the centerline or closer to the stable side. Here, λ_z^+ and λ_x^+ are the spanwise and streamwise wavelength, respectively, in wall units. At all Ro, the spectra of cases 1 and 2 hardly differ up to at least $y = -0.56$, showing that the scalar lengths are not significantly affected by the scalar boundary conditions in this region. Closer to the stable side, on the other hand, the scalar structures are noticeably larger in case 2 for $\mathrm{Ro} = 0.3$ and 0.75 [Figs. 11(c)–11(f)]. This difference in the center region is less obvious at $\mathrm{Ro} = 0$ [Figs. 11(a) and 11(b)]. The spanwise spectra $k_z E_K(k_z)$ and $k_z E_{\theta\theta}(k_z)$ are similar at $\mathrm{Ro} = 0$, in agreement with Antonia *et al.* [3], Brethouwer [10], and the same applies to the streamwise spectra, although the scalar structures appear to be slightly wider than the turbulent scales away from the wall [Figs. 11(a) and 11(b)]. The strong correspondence near the wall is mostly a consequence of the similarity between the streamwise velocity and scalar field, whereas further away from the wall $k_i E_{\theta\theta}(k_i)$ shows a closer correspondence with $k_i E_K(k_i)$ than with the spectra of the streamwise velocity, as noted by Antonia *et al.* [3]. The spanwise as well as the streamwise scalar and turbulence spectra at $\mathrm{Ro} = 0.3$ are still very similar at $y^+ \approx 11$, but at $y^+ \approx 95$ differences are noticeable and at $y = -0.56$ the scalar spectra are clearly more shifted toward longer wavelengths than the turbulent spectra [Figs. 11(c) and 11(d)], implying that the scalar field contains larger structures than the turbulent field. The differences become more pronounced at $\mathrm{Ro} = 0.75$ when also the scalar scales at $y^+ \approx 95$ are longer and wider than the turbulent scales [Figs. 11(e) and 11(f)]. Also closer to the stable channel side at $y = 0.24$ and 0.42 the scalar scales in case 2 are substantially larger than the turbulent scales if $\mathrm{Ro} = 0.3$ and 0.75, whereas in case 1 they are more similar. Near the wall at $y^+ \approx 11$ the scalar scales are by contrast slightly narrower and shorter than the turbulent scales. The peak of $k_z E_{\theta\theta}(k_z)$ at $y^+ \approx 95$ and in the outer region at $\mathrm{Ro} = 0.3$ and 0.75 is at wavelengths wider than $\lambda_z = h$, demonstrating that the scalar field in rotating channel flow contains large structures. Rotation causes thus not only differences in the momentum and scalar transfer but also in the size of scalar and turbulence structures.

It has been shown that the mean turbulent kinetic energy dissipation rate ε and mean scalar dissipation rate ε_θ of scalar variance $\overline{\theta\theta}/2$ become independent of the viscosity and diffusivity at sufficiently high Reynolds numbers [30]. This implies that $\varepsilon\ell/\upsilon^3$ should become constant at high Reynolds numbers if ℓ and υ are turbulent length and velocity scales, respectively, that are independent of the viscosity. Similarly, $\varepsilon_\theta\ell/\upsilon\theta^2$ should become constant too in that case. Donzis *et al.* [30] and Abe and Antonia [31] show that these ratios are approximately constant in isotropic turbulence and nonrotating channel flow away from the wall, respectively, in agreement with these predictions, but an open question is if these ratios are independent of rotation. To answer this question, appropriate length and velocity scales have to be defined at first. Since in nonrotating channel flow E_K and $E_{\theta\theta}$ are similar, as shown before, it appears that $L_q = L_{uu} + L_{vv} + L_{ww}$ and

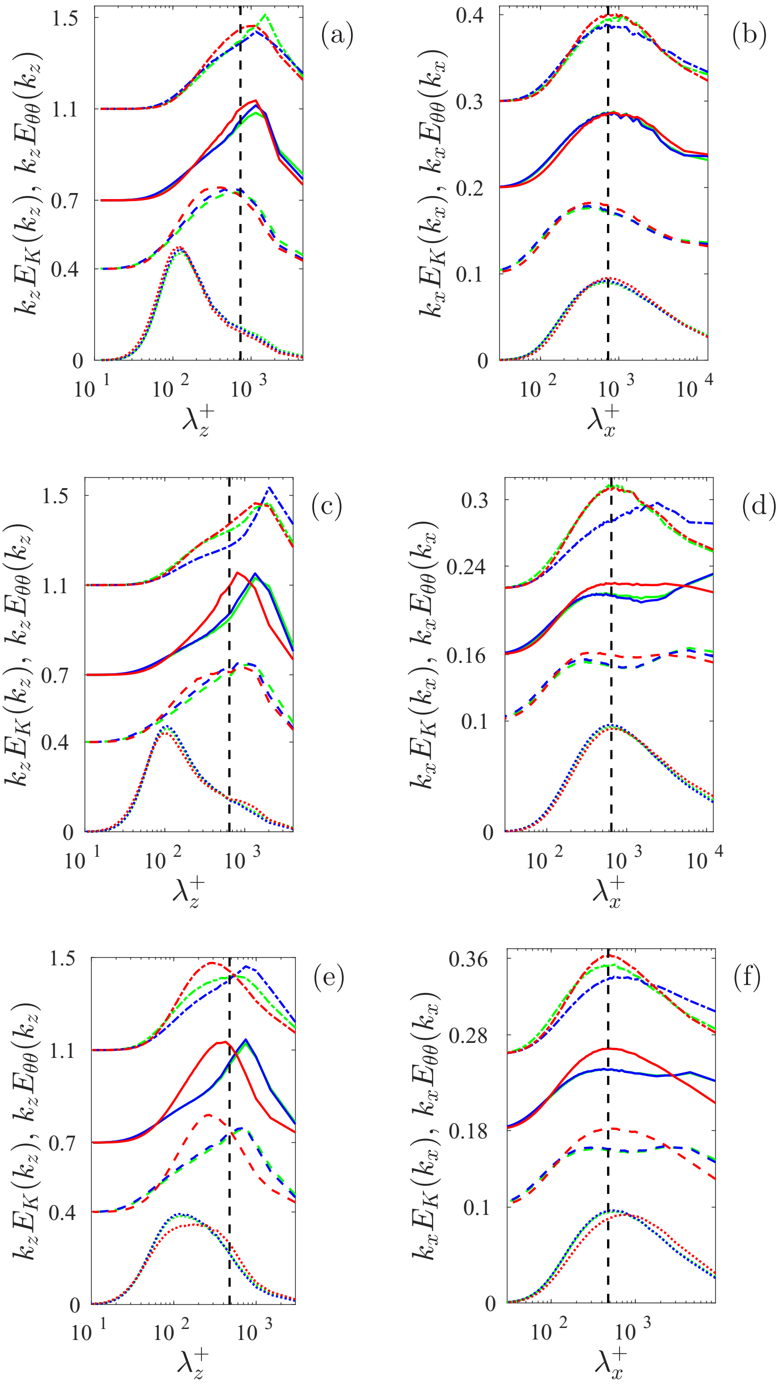

FIG. 11. Premultiplied one-dimensional [(a), (c), (e)] spanwise spectra as a function of λ_z^+ and [(b), (d), (f)] streamwise spectra as a function of λ_x^+ at Ro = 0 [(a), (b)], Ro = 0.3 [(c), (d)], and Ro = 0.75 [(e), (f)]. Shown are spectra at $y^+ \approx 11$ (dotted lines), $y^+ \approx 95$ (dashed lines), and $y = -0.56$ (solid lines) shifted in the vertical with an offset. Also spectra (dash-dotted lines) at $y = 0$, 0.42, and 0.24 for $R = 0$, 0.3, and 0.75, respectively, are shown. The red lines show $k_i E_K(k_i)$ and the green and blue lines $k_i E_{\theta\theta}(k_i)$ for case 1 and 2, respectively.

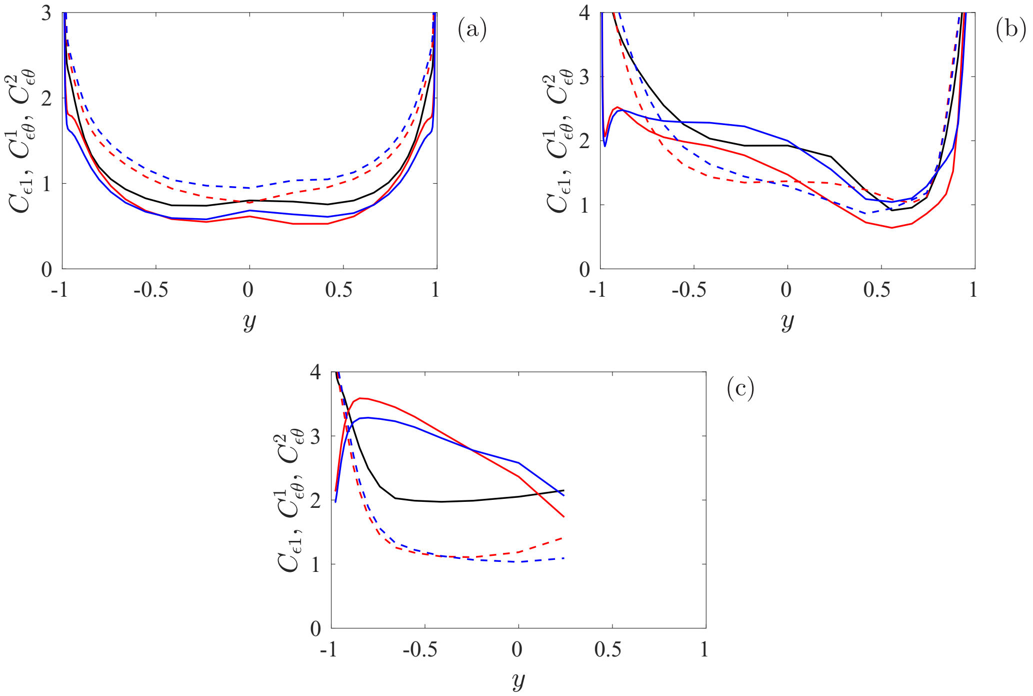

FIG. 12. $C_{\epsilon 1}$ (black solid); $C^1_{\epsilon\theta}$ (solid); $C^2_{\epsilon\theta}$ (dashed). Red: θ_1; blue: θ_2. (a) Ro $= 0$, (b) Ro $= 0.3$, and (c) Ro $= 0.75$.

$L_{\theta\theta}$ are appropriate length scales. Here,

$$L_{uu} = \int_0^\infty R_{uu} dr, \quad R_{uu}(r) = \frac{\overline{u(x+r)u(r)}}{u'^2}, \tag{9}$$

and similarly for the other velocity components and scalars. To compute the length scales the two-point correlations are integrated up to the first zero crossing point or $L_x/2$ if the correlation remains positive. Using these length scales, the following nondimensional parameters can be defined:

$$C_{\epsilon 1} = \varepsilon L_{qq}/(u' q'^2), \quad C^1_{\epsilon\theta} = \varepsilon_\theta L_{\theta\theta}/(u'\theta'^2), \tag{10}$$

where $q'^2 = \overline{u_i u_i}$ [31]. Another nondimensional parameter for the scalar dissipation rate that can be defined is

$$C^2_{\epsilon\theta} = \varepsilon_\theta L_{qq}/(u'\theta'^2). \tag{11}$$

Figure 12 shows $C_{\epsilon 1}$, and $C^1_{\epsilon\theta}$ and $C^2_{\epsilon\theta}$ for both scalar cases at Ro $= 0, 0.3$, and 0.75. The parameters are not shown for the stable side at Ro $= 0.75$ because the length scales are ill defined when the flow relaminarizes. Abe and Antonia [31] found that $C_{\epsilon 1}$ and $C^1_{\epsilon\theta}$ are fairly constant away from the wall in nonrotating channel flow with $C_{\epsilon 1}$ being slightly larger than $C^1_{\epsilon\theta}$. The present results at Ro $= 0$ are in agreement with this finding; moreover, they show that $C^1_{\epsilon\theta}$ is nearly the same for the two scalar cases. Also the profiles of $\varepsilon_\theta/\theta'^2$ (not shown) are similar, although the profiles of ε_θ differ. The results suggest that the timescale of the scalar dissipation rate has a similar relation to the large-scale timescale $L_{\theta\theta}/u'$ in the two cases. Another timescale ratio used in modeling is $r = \theta'^2\varepsilon/(q'^2\varepsilon_\theta)$. In case 2 it varies between 0.5 and 0.56 in the center region (not shown), in good agreement with Béguier *et al.* [32] and Abe and Antonia [31], whereas in case 1 it is between 0.55 and 0.7 and thus larger, but not very much. The smaller scalar scales apparently share similarities in the two cases and the same modeling assumptions can be used even though the scalar fluctuations and mean scalar gradients are vastly different in the center region. Also $C^2_{\epsilon\theta}$ is fairly constant in the center region but larger. At $\text{Ro} = 0.3$ and 0.75 both $C_{\epsilon 1}$ and $C^1_{\epsilon\theta}$ are clearly larger on the unstable side and $C_{\epsilon 1}$ and $C^1_{\epsilon\theta}$ show larger changes with Ro than $C^2_{\epsilon\theta}$. There is also a larger difference between $C_{\epsilon 1}$ and $C^1_{\epsilon\theta}$ and $C^1_{\epsilon\theta}$ for the two scalars differ more. Moreover, $C^1_{\epsilon\theta}$ varies considerably with y at $\text{Ro} = 0.75$, in contrast to $C_{\epsilon 1}$ and $C^2_{\epsilon\theta}$, which are more constant. This shows that $C_{\epsilon 1}$ and $C^1_{\epsilon\theta}$ may become independent of the viscosity and diffusivity at sufficiently high Reynolds number but not of the rotation rate. Only $C^2_{\epsilon\theta}$ varies less with Ro, demonstrating that the choice of the length scale is crucial.

VII. CONCLUSIONS

Passive scalar transport in fully developed turbulent channel flow subject to spanwise rotation is studied with the help of DNS. At high Ro the flow partly relaminarizes on the stable channel side. Two scalar cases are considered; in the first case the scalar transport is driven by an assigned scalar difference at the walls resulting in a mean wall-normal scalar gradient; in the second case the scalar transport is forced by a constant mean streamwise scalar gradient. The aim is to further study the influence of rotation and also the influence of scalar boundary conditions on the scalar transport in channel flow.

In the second case with the imposed mean streamwise gradient the mean scalar flux at the wall on the unstable and stable sides grows and decays with Ro, respectively, and rotation reduces the streamwise turbulent scalar flux in the outer region and Nusselt number. Although the mean, fluctuations, and turbulent flux of the scalar obviously differ in the two cases with different boundary conditions, they are mostly similar near the wall in terms of wall units. Also the scalar spectra are similar, at least up to $y = -0.56$ on the unstable channel side. On the other hand, closer to the center there are differences in the two cases. Scalar fluctuations and the turbulent Prandtl number are then smaller in the case with the mean streamwise scalar gradient, implying that the turbulent momentum and scalar transport differ more. This could be related to the small wall-normal mean scalar gradient in that case, as suggested by Abe and Antonia [20]. The scalar scales in the center region near the stable side in rotating channel flow are also substantially larger in the case with the mean streamwise scalar gradient. On the other hand, the timescale of the scalar dissipation rates is quite similar in the outer region, suggesting that the scalar has the same small-scale properties in the two cases.

Brethouwer [10] showed that there is no Reynolds analogy for scalar-momentum transfer in rotating channel flow in the case with the assigned scalar difference at the walls. This result is basically not affected by the scalar boundary conditions. Also in the case with an imposed mean streamwise scalar gradient the turbulent Prandtl number is much smaller than unity on the unstable channel side in rotating channel flow, showing that turbulent scalar transfer is much faster than momentum transfer. Moreover, the scalar structures are larger than turbulence structures in rotating channel flow in the outer region of the unstable side. This is in obvious contrast to nonrotating channel flow for which the Reynolds analogy is valid with the exception of the center region where the difference between momentum and scalar transfer is larger in the case with the mean streamwise scalar gradient. More differences for that case are discussed by Antonia *et al.* [3], Abe and Antonia [20]. The clear failure of the Reynolds analogy for $\text{Ro} > 0$ stems from the different influence of rotation on the turbulent scalar flux compared to the Reynolds shear stress. Rotation induces a Coriolis term $-2\Omega(\overline{u^2} - \overline{v^2})$ in the governing equation of $\overline{uv}$ but a different Coriolis term $-2\Omega\overline{u\theta}$ in the governing equation of $\overline{v\theta}$. As a result, rotation slows down the scalar transfer in turbulent channel flow, as shown by the declining Nusselt numbers, but the momentum transfer decays even faster with Ro, with the result that the turbulent scalar transfer is rapid compared to momentum transfer. A similar phenomenon, rapid heat compared to momentum transfer, was observed by Pirozzoli *et al.* [33] in their DNS of mixed convection in turbulent channel flows at sufficiently high Richardson numbers. They speculated that this difference was caused by the large roll cells found in their DNS. Large roll cells are also observed in the present DNS at moderate Ro, indicating that these roll cells indeed could play a role in the breakdown of the Reynolds analogy. However, Brethouwer [10] also observed low turbulent Prandtl numbers at $\mathrm{Ro} = 0.9$ and 1.2 when large roll cells are absent, showing that these large-scale structures are not a prerequisite for efficient heat transfer. Motoki *et al.* [34] showed theoretically through an optimization study that certain structures like quasistreamwise near-wall vortices induce very efficient heat transport compared to momentum transport in a wall-bounded flow. In future studies it could be of interest to examine if there are similarities between these structures and those in rotating channel flow.

ACKNOWLEDGMENTS

SNIC is acknowledged for providing computational resources in Sweden. The author further acknowledges financial support from the Swedish Research Council (Grant No. 621-2016-03533).

[1] S. Pirozzoli, M. Bernardini, and P. Orlandi, Passive scalars in turbulent channel flow at high Reynolds number, J. Fluid Mech. **788**, 614 (2016).
[2] H. Abe and R. A. Antonia, Near-wall similarity between velocity and scalar fluctuations in turbulent channel flow, Phys. Fluids **21**, 025109 (2009).
[3] R. A. Antonia, H. Abe, and H. Kawamura, Analogy between velocity and scalar fields in a turbulent channel flow, J. Fluid Mech. **628**, 241 (2009).
[4] Y. Nagano and H. Hattori, Direct numerical simulation and modelling of spanwise rotating channel flow with heat transfer, J. Turbulence **4**, 010 (2003).
[5] N.-S. Liu and X.-Y. Lu, Direct numerical simulation of spanwise rotating turbulent channel flow with heat transfer, Int. J. Numer. Meth. Fluids **53**, 1689 (2007).
[6] Z. Xia, Y. Shi, and S. Chen, Direct numerical of turbulent channel flow with spanwise rotation, J. Fluid Mech. **788**, 42 (2016).
[7] G. Brethouwer, Statistics and structure of spanwise rotating turbulent channel flow at moderate Reynolds numbers, J. Fluid Mech. **828**, 424 (2017).
[8] H. Wu and N. Kasagi, Turbulent heat transfer in a channel with arbitrary directional system rotation, Int. J. Heat Mass Transfer **47**, 4579 (2004).
[9] X. Fang and B.-C. Wang, On the turbulent heat transfer in a square duct subjected to spanwise system rotation, Int. J. Heat Fluid Flow **71**, 220 (2018).
[10] G. Brethouwer, Passive scalar transport in rotating turbulent channel flow, J. Fluid Mech. **844**, 297 (2018).
[11] G. Brethouwer, The effect of rotation on rapidly sheared homogeneous turbulence and passive scalar transport, J. Fluid Mech. **542**, 305 (2005).
[12] S. C. Kassinos, B. Knaepen, and D. Carati, The transport of a passive scalar in magnetohydrodynamic turbulence subjected to mean shear and frame rotation, Phys. Fluids **19**, 015105 (2007).
[13] T.-M. Liou and C.-S. Wang, Large eddy simulation of rotating turbulent flows and heat transfer by the lattice Boltzmann method, Phys. Fluids **30**, 015106 (2018).
[14] Z. Jiang, Z. Xia, Y. Shi, and S. Chen, Large eddy simulation of spanwise rotating turbulent channel flow with dynamic variants of eddy viscosity model, Phys. Fluids **30**, 040909 (2018).
[15] H. Hattori, N. Ohiwa, M. Kozuka, and Y. Nagano, Improvement of the nonlinear eddy diffusivity model for rotational turbulent heat transfer at various rotating axes, Fluid Dyn. Res. **41**, 012402 (2009).
[16] H. Müller, B. A. Younis, and B. Weigand, Development of a compact explicit algebraic model for the turbulent heat fluxes and its application in heated rotating flows, Int. J. Heat Mass Transfer **86**, 880 (2015).
[17] A. Hsieh, S. Biringen, and A. Kucala, Simulation of rotating channel flow with heat transfer: Evaluation of closure models, ASME J. Turbomach. **138**, 111009 (2016).

[18] J. Kim and P. Moin, Transport of passive scalars in a turbulent channel flow, in *Turbulent Shear Flows 6*, edited by J.-C. André, J. Cousteix, F. Durst, B. E. Launder, F. W. Schmidt, and J. H. Whitelaw (Springer, New York, 1989), p. 85.

[19] N. Kasagi, Y. Tomita, and A. Kuroda, Direct numerical simulation of passive scalar field in a turbulent channel flow, ASME J. Heat Transfer **1114**, 598 (1992).

[20] H. Abe and R. A. Antonia, Relationship between the heat transfer law and the scalar dissipation function in a turbulent channel flow, J. Fluid Mech. **830**, 300 (2017).

[21] F. Lluesma-Rodrígez, S. Hoyas, and M. J. Perez-Quiles, Influence of the computational domain on DNS of turbulent heat transfer up to $\mathrm{R}e_\tau = 2000$ and $\mathrm{Pr} = 0.71$, Int. J. Heat Mass Transfer **122**, 983 (2018).

[22] H. Kawamura, H. Abe, and K. Shingai, DNS of turbulence and heat transfer in a channel with different Reynolds and Prandtl numbers and boundary conditions, in *Proceedings of the Third International Symposium on Turbulence, Heat and Mass Transfer*, edited by Y. Nagano (Engineering Foundation, Aichi Shuppan, 2000), p. 15.

[23] A. V. Johansson and P. M. Wikström, DNS and modelling of passive scalar transport in turbulent channel flow with a focus on scalar dissipation rate modelling, Flow Turbulence Combust. **63**, 223 (1999).

[24] H. Kawamura, K. Ohsaka, H. Abe, and K. Yamamoto, DNS of turbulent heat transfer in channel flow with low to medium-high Prandtl number fluid, Int. J. Heat Fluid Flow **19**, 482 (1998).

[25] M. Lee and R. D. Moser, Direct numerical simulation of turbulent channel flow up to $\mathrm{Re}_\tau \approx 5200$, J. Fluid Mech. **774**, 395 (2015).

[26] Y. Duguet, P. Schlatter, and D. S. Henningson, Formation of turbulent patterns near the onset of transition in plane Couette flow, J. Fluid Mech. **650**, 119 (2010).

[27] G. Brethouwer, Y. Duguet, and P. Schlatter, Turbulent-laminar coexistence in wall flows with Coriolis, buoyancy or Lorentz forces, J. Fluid Mech. **704**, 137 (2012).

[28] G. Brethouwer, Linear instabilities and recurring bursts of turbulence in rotating channel flow simulations, Phys. Rev. Fluids **1**, 054404 (2016).

[29] O. Grundestam, S. Wallin, and A. V. Johansson, Direct numerical simulations of rotating turbulent channel flow, J. Fluid Mech. **598**, 177 (2008).

[30] D. A. Donzis, K. R. Sreenivasan, and P. K. Yeung, Scalar dissipation rate and dissipative anomaly in isotropic turbulence, J. Fluid Mech. **532**, 199 (2005).

[31] H. Abe and R. A. Antonia, Scaling of normalized mean energy and scalar dissipation rates in a turbulent channel flow, Phys. Fluids **23**, 055104 (2011).

[32] C. Béguier, I. Dekeyser, and B. E. Launder, Ratio of scalar and velocity dissipation time scales in shear flow turbulence, Phys. Fluids **21**, 307 (1978).

[33] S. Pirozzoli, M. Bernardini, R. Verzicco, and P. Orlandi, Mixed convection in turbulent channels with unstable stratification, J. Fluid Mech. **821**, 482 (2017).

[34] S. Motoki, G. Kawahara, and M. Shimizu, Optimal heat transfer enhancement in plane Couette flow, J. Fluid Mech. **835**, 1157 (2018).